PCCP

Using Metal Substrates to Enhance the Reactivity of Graphene towards Diels-Alder Reactions

Journal:	*Physical Chemistry Chemical Physics*
Manuscript ID	CP-ART-04-2022-001842.R2
Article Type:	Paper
Date Submitted by the Author:	07-Jul-2022
Complete List of Authors:	Yang, Xiaojian; University of Massachusetts Lowell Chen, Feiran ; University of Massachusetts Lowell Kim, Min A; University of Pittsburgh Liu, Haitao; University of Pittsburgh Wolf, Lawrence ; University of Massachusetts Lowell Yan, Mingdi; University of Massachusetts Lowell

ARTICLE

Using Metal Substrates to Enhance the Reactivity of Graphene towards Diels-Alder Reactions

Received 00th January 20xx,
Accepted 00th January 20xx

DOI: 10.1039/x0xx00000x

Xiaojian Yang,[#ab] Feiran Chen,[#a] Min A. Kim,[c] Haitao Liu,[*c] Lawrence M. Wolf[*a] Mingdi Yan[*a]

The Diels-Alder (DA) reaction, a classic cycloaddition reaction involving a diene and a dienophile to form a cyclohexene, is among the most versatile organic reactions. Theories have predicted thermodynamically unfavorable DA reactions on pristine graphene owing to its low chemical reactivity. We hypothesized that metals like Ni could enhance the reactivity of graphene towards the DA reactions through charge transfer. Results indeed showed that metal substrates enhanced the reactivity of graphene in the DA reactions with a diene, 2,3-dimethoxy butadiene (DMBD), and a dienophile, maleic anhydride (MAH), with the activity enhancement in the order of Ni>Cu, and both are more reactive than graphene supported on silicon wafer. The rate constants were estimated to be twice higher for graphene supported on Ni than on silicon wafer. The computational results support the experimentally obtained rate trend of Ni>Cu, both predicted to be greater than unsupported graphene, which is explained by enahnced graphene-substrate interaction reflected in charge transfer effects with the strongly interacting Ni. This study opens up a new avenue for enhancing the chemical reactivity of pristine graphene through substrate selection.

Introduction

Chemical functionalization of graphene can introduce well-defined functional groups, open bandgap, and enable the integration of graphene into high performance composite materials and devices.[1-6] Since graphene contains exclusively sp^2 carbons, the large resonance stabilization makes it chemically inert, which poses considerable challenges to carry out chemical reactions on graphene. As such, the covalent chemistry on pristine graphene requires highly reactive species such as free radicals, carbenes and nitrenes.[7] A grand challenge in graphene chemistry is to expand the chemical space and enable a wide range of reactions on graphene. To meet this challenge, innovative strategies are needed to enhance the reactivity of pristine graphene. Like many nanoscale materials, the graphitic edges of graphene are more reactive than its basal plane due to the presence of dangling bonds on the edges. Thus, one way to increase the reactivity of graphene is to increase the number of edges and defect sites on graphene. Different methods, including lithography, have been used to intentionally create holes in the basal plane to make the so-called holey graphene or graphene nanomeshes.[8, 9] Methods have also been explored to enhance the reactivity of pristine graphene through substrate manipulation without compromising the integrity of the graphene material. For example, reaction with aryl radicals was observed in the regions of monolayer graphene deposited on top of silica nanoparticles.[10] Substrates that can induce large charge fluctuations have been used to increase the reactivity of graphene with diazonium salt.[11] Charge doping of graphene, both positive and negative, was also employed to enhance the reactivity of graphene towards the oxidation reaction.[12] In this case, graphene supported on a dielectric substrate was heated photothermally in air to induce the oxidation reaction of graphene while an electric field was applied.

The Diels-Alder (DA) reaction, a classic cycloaddition reaction involving a diene and a dienophile to form a cyclohexene moiety, is among the most versatile organic reactions. It can be carried out under mild conditions, gives high product yields, has 100% atom economy, and could be considered as a click reaction.[13] As the reaction converts sp^2 carbons to sp^3, it introduces covalent defects and opens a bandgap in graphene.[14, 15] Furthermore, most DA reactions are reversible, therefore, the functionalized product can in principle be converted back to pristine graphene, done under different reaction conditions, to regain its original structure and properties. The first example of DA reactions on graphene was reported by Haddon and coworkers, demonstrating that graphene could act as both a diene and a dienophile.[16] The authors also showed that the reaction applied to a variety of graphene materials, including exfoliated and epitaxial graphene as well as highly ordered pyrolytic graphite (HOPG). Subsequent density functional theory (DFT) calculations by

[a.] *Department of Chemistry, University of Massachusetts Lowell, 1 University Ave., Lowell, MA 01854. E-mail: Mingdi_Yan@uml.edu, Lawrence_Wolf@uml.edu*
[b.] *China Aerospace Science and Industry Corporation Limited, 40 Yungangbeili, Beijing, China 100074.*
[c.] *Department of Chemistry, University of Pittsburgh, 4200 Fifth Ave, Pittsburgh, PA 15260. E-mail: hliu@pitt.edu.*
[#.] *These authors contributed equally to this work.*
†Electronic Supplementary Information (ESI) available: [details of any supplementary information available should be included here]. See DOI: 10.1039/x0xx00000x

Houk and coworkers gave high endothermic energies of 40 – 42.5 kcal/mol for the DA reactions on the basal plane of graphene, which led to the conclusion that the reactions likely took place on defects and edges rather than on the basal plane of graphene.[17, 18] Other computational studies also emphasized the high endothermic energies (~47 – ~63 kcal/mol) for the DA reactions on pristine graphene.[19,20]

While contradictions remain between the experimental results and computations, the DA reactions continue to attract attention from researchers. For example, Wan and coworkers reported the DA reaction of graphene with a diene, 7,7'-dimethoxy-3,3',4,4'-tetrahydro-1,1'-binaphthalene.[21] Kinetic studies yielded an activation barrier as low as 13 kJ/mol, and the reaction was thought to proceed like a click type reaction. Berndt and coworkers reported a cycloaddition reaction of iron phthalocyanine with graphene supported on Ir.[22] The reaction was slightly endothermic, making the reaction feasible at high temperature. The enhanced reactivity of graphene was attributed to the Ir substrate, which created unsaturated dangling bonds located on C atoms in hollow sites of the Ir lattice. Simon and coworkers carried out a room temperature DA reaction between a fluorinated maleimide and graphene supported on SiC (0001).[23] In this case, graphene acted as a diene, and reacted with the maleimide dienophile activated by the six F atoms.

We hypothesize that metal substrates would enhance the reactivity of graphene towards DA reactions by altering the electron density in graphene. Metals like Ni and Cu have shown to induce changes in the electron density and charge distribution in graphene.[24] For example, the *d* orbitals of Ni overlap with the *p* electrons in graphene, resulting in strong interactions between Ni and graphene.[25-27] The equilibrium separation between graphene and Ni was reported to be 2.07 Å, far less than other metals like Cu (2.96 Å) or Ir (3.44 Å).[28] Consequently, both the physical and chemical properties of graphene can be significantly altered. We previously found that graphene supported on Ni was more reactive towards perfluorophenyl nitrene than graphene supported on Cu, and graphene supported on silicon wafer was the least reactive.[29] DFT calculations suggest that the metal substrate stabilizes the physisorbed nitrene through enhanced electron transfer to the singlet nitrene from the graphene surface assisted by the electron rich metal substrate.

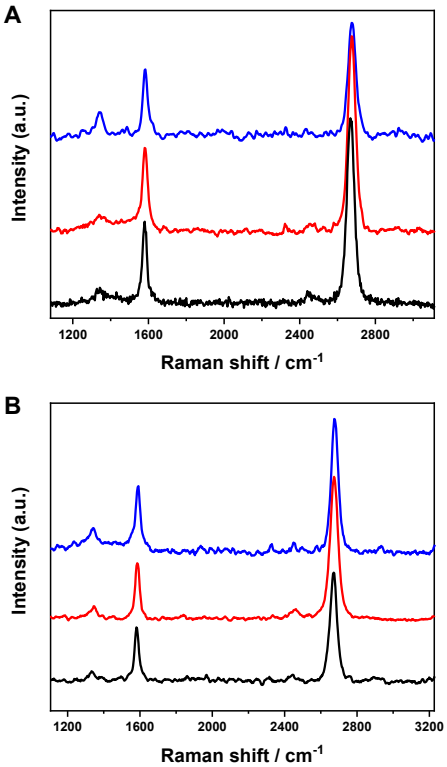

Fig. 1 Raman I_D/I_G vs. reaction time at different temperatures for DA reaction between DMBD and (A) G/Ni, (B) G/Cu, or (C) G/SiO_2/Si. (D) 3D bar chart of I_D/I_G vs. reaction time and temperature. For G/Ni or G/Cu, the graphene films were transferred to silicon wafers prior to taking the Raman spectra. Data in (A) – (C) were collected from ~400 spots on 2 sets of independent samples.

A diene, 2,3-dimethoxy butadiene (DMBD), and a dienophile, maleic anhydride (MAH), were chosen as the model reagents in this work (Scheme 1). DMBD and MAH have been used in the DA reactions with HOPG, epitaxial graphene, and mechanical exfoliated few-layer graphene flakes.[30] In this study, graphene supported on Ni (G/Ni), Cu (G/Cu), or silicon wafer (G/SiO_2/Si) were allowed to react with DMBD or MAH, and the products were characterized by Raman spectroscopy and Raman imaging. Results showed that Ni as the substrate indeed enhanced the reactivity of graphene towards DA reactions. DFT calculations supported the experimental results.

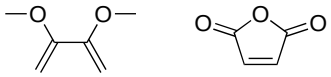

Scheme 1 Diene DMBD and dienophile MAH used in this study.

Results and Discussion

Fabrication of substrate-supported graphene

Monolayer graphene was first prepared on Cu foils by chemical vapor deposition (CVD), and then transferred to Ni or Cu substrate. Prior to graphene deposition, Cu foils were electropolished to remove surface contaminants and to reduce surface roughness.[31] CVD graphene was synthesized in a tube furnace by heating at 1000 °C under Ar/H_2 for 60 min, and then Ar/H_2/CH_4 for 60 min before cooling to room temperture.[29]

CVD graphene on Cu foil was transferred to Ni or Cu films or silicon wafers using the poly(methyl methacrylate) (PMMA)-assisted protocol following our previous procedure.[29, 32] The quality of each batch of graphene samples was checked by Raman spectroscopy. Only those that showed the characteristic narrow G band and symmetrical 2D band, corresponding to the typical monolayer graphene, were used in the subsequent studies.[33, 34] To confirm that the transfer process did not create additional defects in graphene, graphene on Ni or Cu were again transferred to silicon wafers and the samples examined by Raman spectroscopy.[29]

DA Reactions on substrate-supported graphene

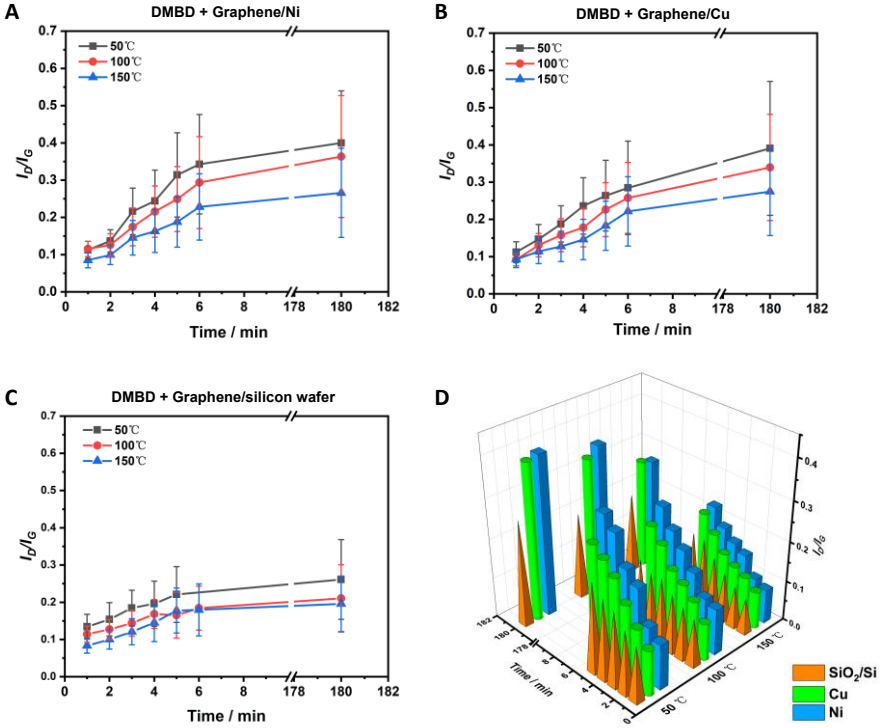

Fig. 2 Representative Raman spectra of DA reactions on G/Ni (blue), G/Cu (red) or G/SiO_2/Si (black): (A) DMBD at 50 °C for 5 min or (B) MAH at 100 °C for 5 min. For G/Ni or G/Cu, graphene was further transferred to silicon wafer for Raman characterization.

The reactions were first carried out by heating G/Ni or G/Cu in the solution containing either the diene or the dienophile. In most cases, especially at elevated temperatures, the graphene films fell off from the substrate. To avoid this issue, we adopted a solvent-free reaction condition by drop-casting a solution of DMBD or MAH in *p*-xylene on the graphene surface followed by heating the samples. Under this condition, the solvent evaporated quickly upon heating. The solvent-free condition has been used in the DA reactions of graphene with binaphthalene up to 220 °C,[21] graphite with MAH or maleimide at 160-220 °C,[35] graphene and graphite with cyclopentadiene derivatives under forces using arrays of AFM tips.[17]

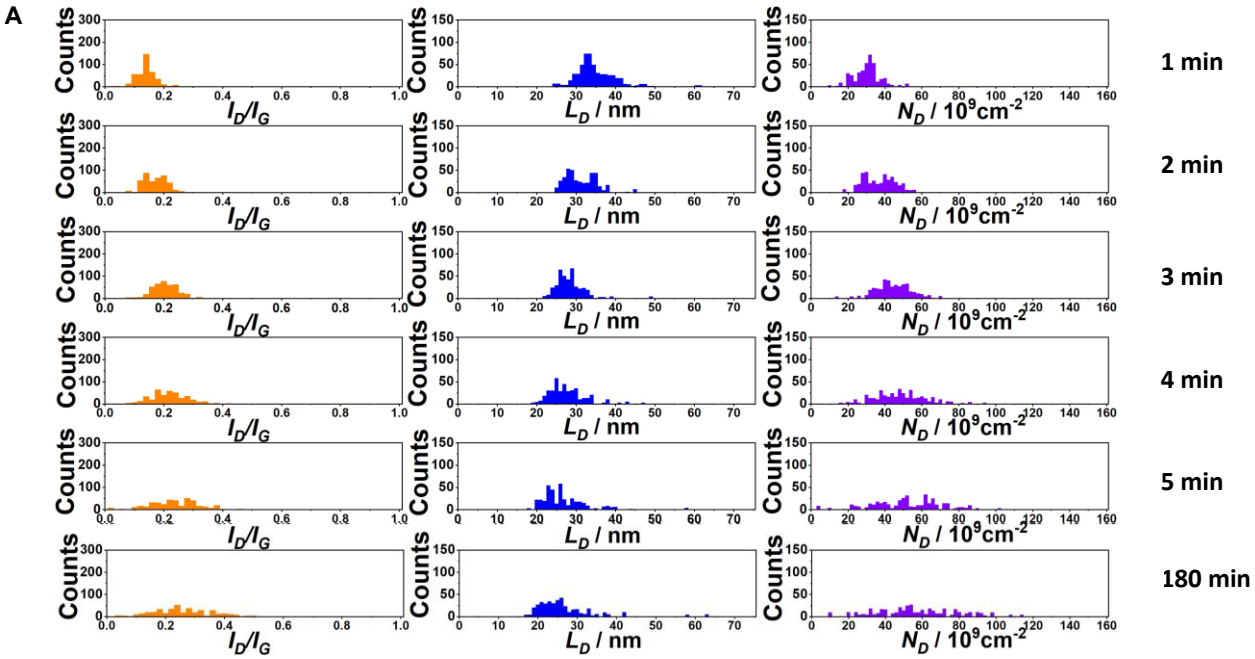

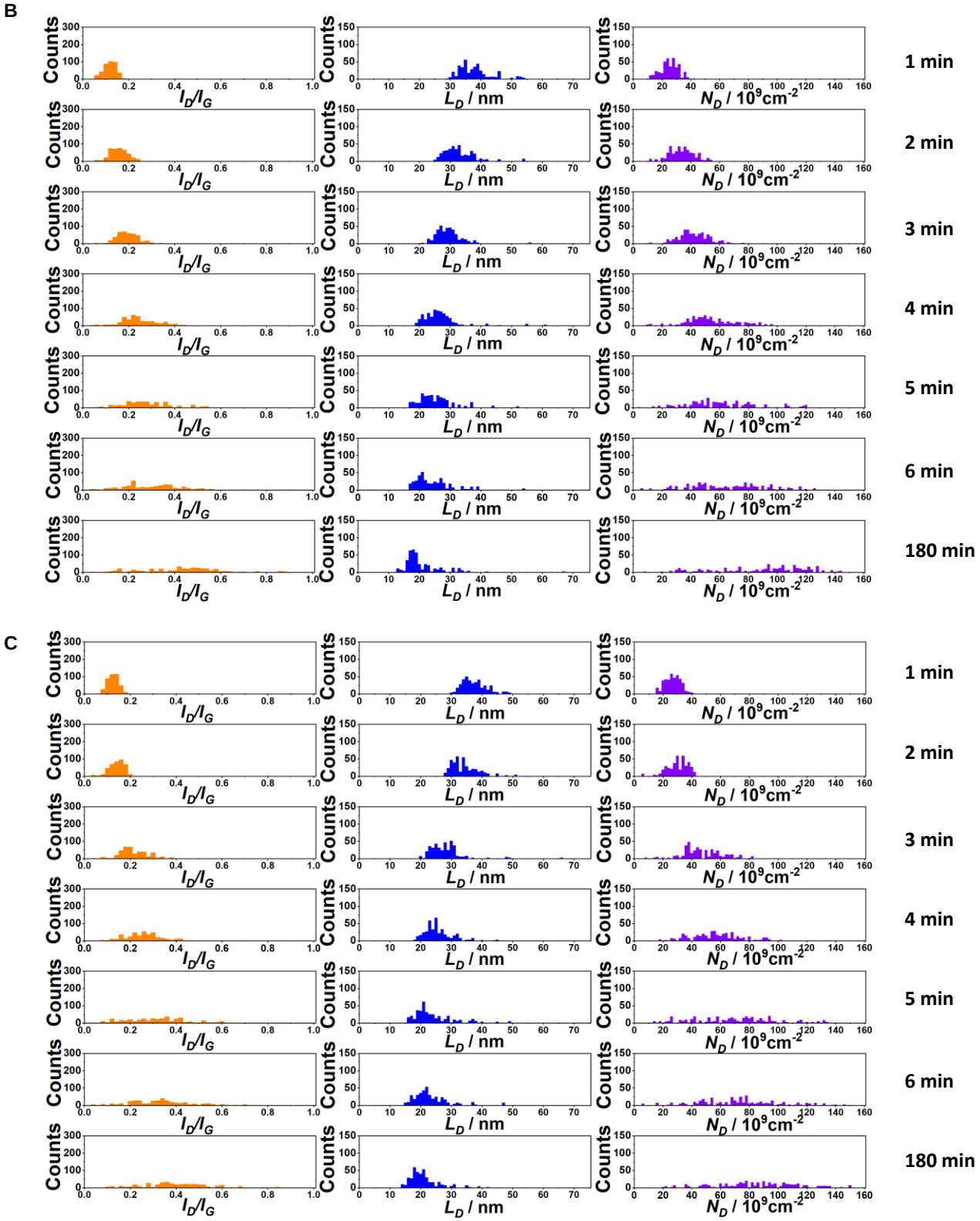

Fig. 3 Histograms of Raman I_D/I_G (left) L_D (middle), and n_D (right) of (A) G/SiO_2/Si, (B) G/Cu, (C) G/Ni after reacting with DMBD at 50 ℃ for different lengths of time. For each set, ~400 data points were collected from 2 independent samples.

DA reactions were carried out by placing a drop of either

DMBD or MAH in *p*-xylene (0.1 M, 10 µL) on the graphene surface, and the samples were heated at 50 or 100 °C for 5 min (boiling points of DMBD and MAH are 136 °C and 202 °C, respectively). The samples were then washed thoroughly with acetone and dried under air flow. After reaction with DMBD or MAH, the characteristic D band at ~1350 cm^{-1} appeared in the Raman spectra of the products (Fig. 1). Furthermore, the intensity of the D band for G/Ni (blue) was the strongest, followed by G/Cu (red) and then G/SiO_2/Si (black). The Raman D band, which is absent in defect-free graphene, becomes activated when sp^2 C is converted to sp^3.[36, 37]

Reaction of DMBD with substrate-supported graphene

The reactions were carried out by placing a drop of DMBD in *p*-xylene (0.1 M, 10 µL) on the graphene surface, and the samples were heated at 50, 100, or 150 °C for 1, 2, 3, 4, 5, 6, or 180 min. At low levels of defects, the intensity ratio of Raman D and G bands (I_D/I_G) can be used to quantify the extent of functionalization on graphene.[38, 39] The I_D/I_G of substrate-supported graphene after reaction with DMBD at different temperatures was plotted against reaction time (Fig. 2A-2C). I_D/I_G increased with reaction time for all graphene samples, more rapidly in the first 6 min than the subsequent 3 hours. The temperature had the opposite effect; the higher the temperature, the lower the I_D/I_G. These data are consistent with those reported by Haddon and coworkers where the highest DA reactivity occurred at lower (e.g., 50 ℃) rather than higher temperatures.[16] In our case, the lower functionalization at higher temperatures especially 150 ℃ could also be due to the evaporation of the reagent (boiling point of DMBD: 136 °C). Nevertheless, the 3D plot of I_D/I_G vs. the reaction time and temperature showed that G/Ni had the highest reactivity at all temperatures tested (Fig. 2D). At 50 ℃, I_D/I_G reached 0.40±0.14 for G/Ni after reacting with DMBD for 3 h.

following two parameters: (1) L_D, the distance between the point defects, and (2) n_D, the defect density, i.e., the number of point defects per cm^2. L_D and n_D of graphene after reaction with DMBD were then computed according to Eqs. 1 and 2 following the literature and our previous method.[29]

$$L_D^2 = (1.8 \pm 0.5) \times 10^{-9} \lambda^4 \left(\frac{I_D}{I_G}\right)^{-1} \quad (1)$$

λ (in nm): the excitation wavelength of the laser, which was 532 nm in our case.

$$n_D = \frac{(10^7\ nm)^2}{\pi (L_D\ nm)^2} = \frac{10^{14}}{\pi {L_D}^2} \quad (2)$$

Fig. 3 are the histograms of I_D/I_G, L_D and n_D of graphene after reaction with DMDB at 50 °C for different times (histograms at all temperatures can be found in Figs. S2-S10. As expected, L_D of all graphene samples are larger than 10 nm. L_D decreased and n_D increased with reaction time, indicating increased functionalization on graphene. As the reaction progressed, the distributions of L_D and n_D broadened, which implies greater heterogeneity. Judging from the distribution of I_D/I_G, which were narrow and of low defects at the beginning of the reaction, became broader with reaction time and the low defect regions were replaced by higher defects spanning from 0.2 to up to over 0.8 for G/Cu (Figs. 3B) and G/Ni (Figs. 3C).

Assuming a pseudo-first order reaction kinetics under the condition of [DMBD] >> [graphene], the pseudo-first order rate constant *k'* can be calculated following Eq. 3 following our previous method.[29]

$$1 - 0.067 \frac{I_D}{I_G} = e^{-k't} \quad (3)$$

Figs. 4A-4C plot -ln[$1 - 0.067 \frac{I_D}{I_G}$] vs. t (min) at 50 ℃, 100 ℃, and 150 ℃, respectively. At each temperature, metal as the

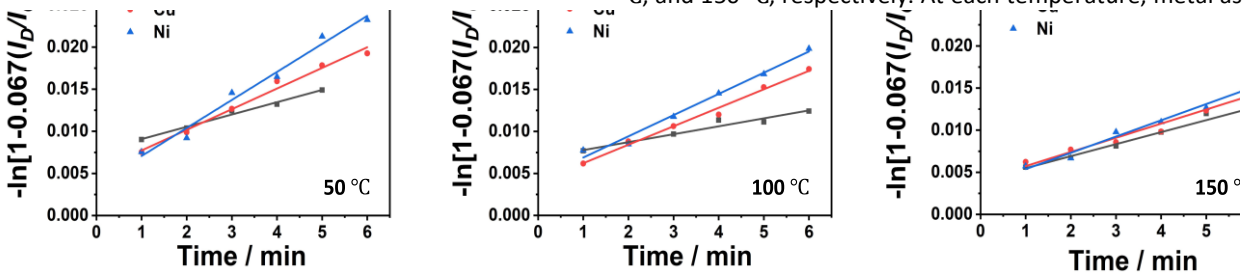

D

k' (min^{-1})	Ni	Cu	SiO_2/Si
50 °C	0.0033±0.0002	0.0024±0.0001	0.0015±0.0001
100 °C	0.0025±0.0001	0.0022±0.0001	0.0014±0.0001
150 °C	0.0019±0.0001	0.0017±0.0001	0.0009±0.0002

Fig. 4 Plots of -*ln*[1-0.067(I_D/I_G)] vs. time for reaction of DMBD with G/Ni (blue), G/Cu (red) or G/SiO_2/Si (grey) at (A) 50 ℃, (B) 100 ℃, and (C) 150 ℃. (D) The apparent rate constants (k', min^{-1}) calculated from Eq. 3.

The extent of functionalization was evaluated using a model developed by Jorio *et al.*[38] In this model, the extent of graphene functionalization can be quantified using the substrate accelerate the reaction, with G/Ni giving the highest rate. For example, the pseudo-first order rate constants for G/Ni were 1.8~2.2 times higher than G/SiO_2/Si (Fig. 4D).

Reaction of MAH with substrate-supported graphene

increasing temperature in the case of MAH. This trend was also observed by Haddon and coworkers.[16] Evaporation of the reagent is of less concern as the boiling point of MAH is much

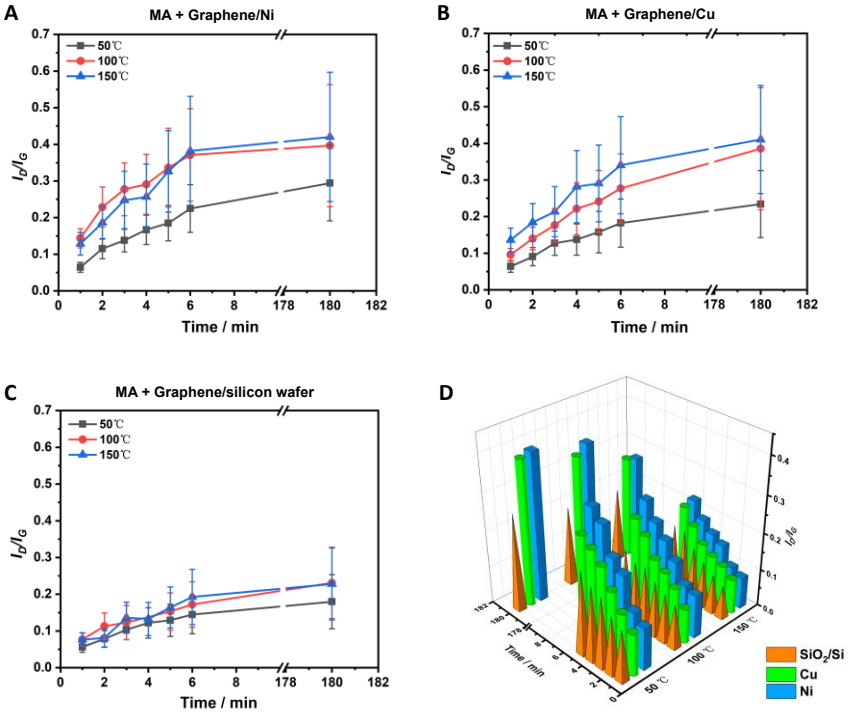

Fig. 5 Raman I_D/I_G vs. reaction time at different temperatures for DA reactions between MAH and (A) G/Ni, (B) G/Cu, or (C) G/SiO_2/Si. (D) 3D bar chart of I_D/I_G vs. reaction time and temperature. For G/Ni or G/Cu, the graphene films were transferred to silicon wafers prior to taking the Raman spectra. Data in (A) – (C) were collected from ~400 spots on 2 sets of independent samples.

Reactions were carried out between substrate-supported graphene and MAH using the same experimental protocols as DMBD under solvent-free conditions. Results are presented in Figs. 5-6. Similar to DMBD, the metal substrates increased the reactivity of graphene towards MAH, with Ni giving the highest degree of functionalization. The pseudo-first order rate constants for G/Ni were 1.8-2.4 times higher than G/SiO_2/Si (Fig. 6D). Contrary to DMBD, the reactivity increased with higher at 202 °C.

The extent of functionalization was calculated following Eqs. 1 and 2 as described above. Fig. 7 are the histograms of I_D/I_G, L_D and n_D of the reaction at 150 °C at different reaction times (histograms at all temperatures can be found in Figs. S11-S19). Similar to the reaction with DMBD, L_D of all samples are larger than 10 nm, L_D decreased and n_D increased and the distributions of L_D and n_D broadened with reaction time.

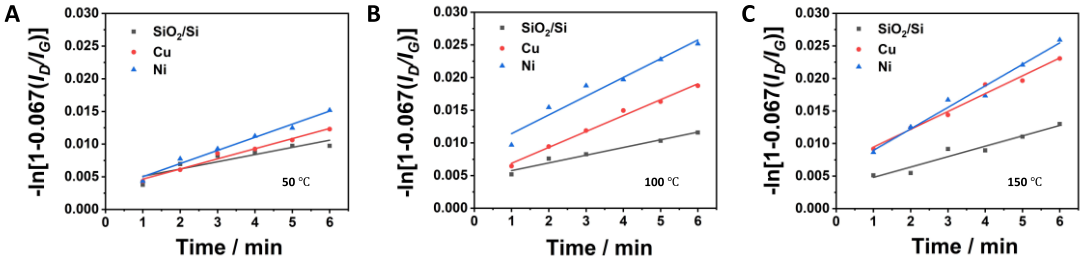

D

k' (min^{-1})	Ni	Cu	SiO_2/Si
50 °C	0.0020±0.0001	0.0015±0.0001	0.0011±0.0002
100 °C	0.0029±0.0003	0.0024±0.0001	0.0012±0.0001
150 °C	0.0033±0.0002	0.0027±0.0002	0.0015±0.0002

Fig. 6 Plots of $-ln[1-0.067(I_D/I_G)]$ vs. time for reactions between MAH and graphene suppported on Ni (blue), Cu (red) or silicon wafer (grey) at (A) 50 °C, (B) 100 °C, and (C) 150 °C. (D) The apparent rate constants (k', min^{-1}) calculated from Eq. 3.

Computational Results.

The reaction was also explored computationally in an effort to gain insight into the nature of the reaction and substrate dependence. DFT calculations were performed using the PBE[40-42] functional with the D2 dispersion correction using ultra-soft pseudopotentials. A 6x6 graphene sheet adsorbed to Cu(111) and Ni(111) metallic substrates was used to model the G/Cu and C/Ni systems respectively while a free-standing graphene sheet (G) was used to model the $G/SiO_2/Si$ system given the weak interaction between graphene and silicon wafer.

The DA reactions between graphene and MAH and DMBD were explored on different substrates. The predicted reaction energy diagrams for the DA reaction with MAH on graphene (G), for graphene on Cu(111) (G/Cu) and for graphene on Ni(111) (G/Ni) is given in Fig. 8. The corresponding geometries are provided in Fig. 10 using Cu and Ni. The MAH is first allowed to physisorb to the graphene surface to form INT from the initial state, IS, at infinite separation. The MAH physisorbs more strongly to the G/Ni system over the G/Cu and G systems, by roughly 7-8 kcal·mol^{-1}. The physiorbed MAH then undergoes the DA reaction to the graphene surface to form the [4+2] products FS. The energy barrier is predicted to be much lower on the G/Ni system (23.0 kcal·mol^{-1}) than in the G/Cu (46.8 kcal·mol^{-1}) systems. The much more strongly

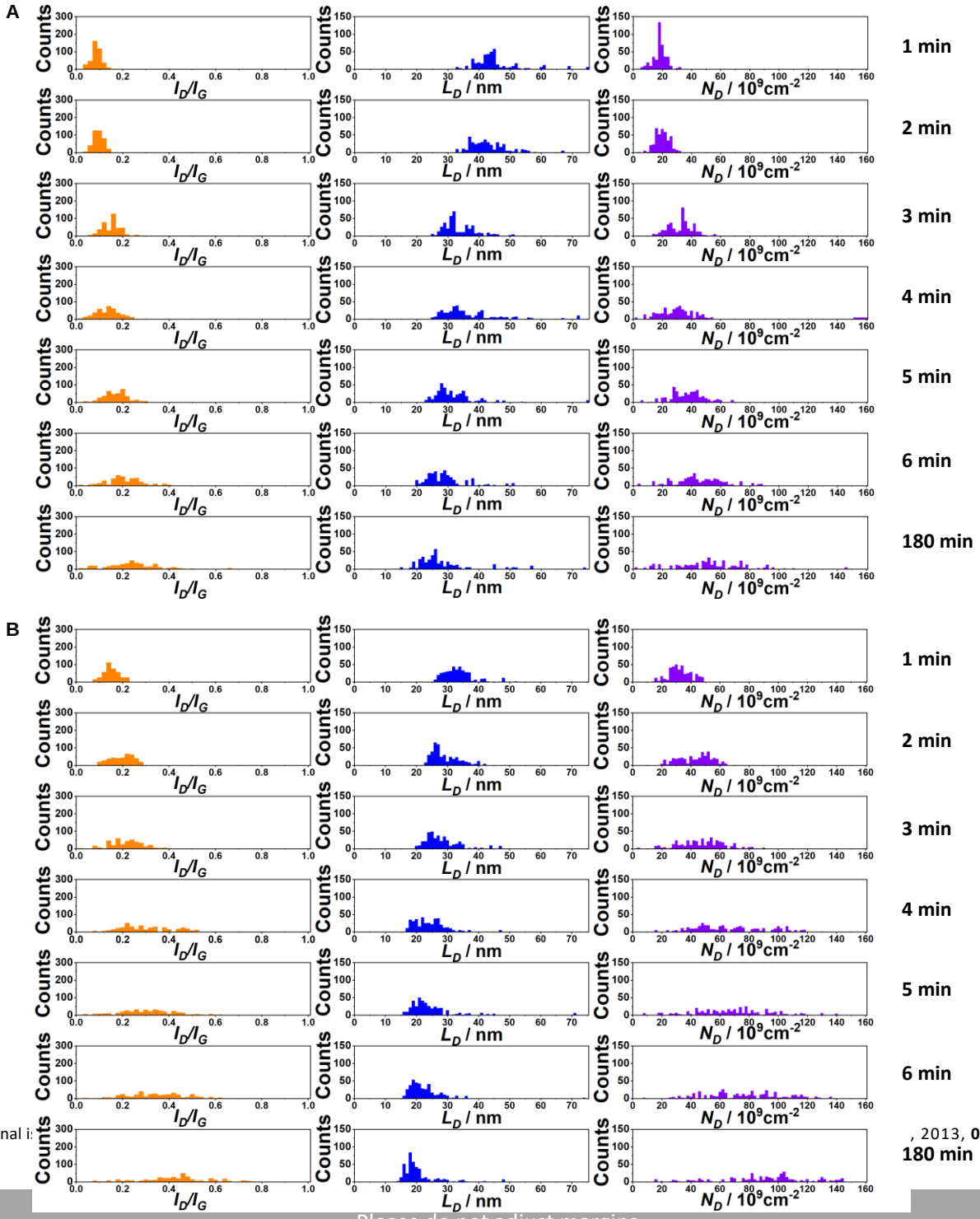

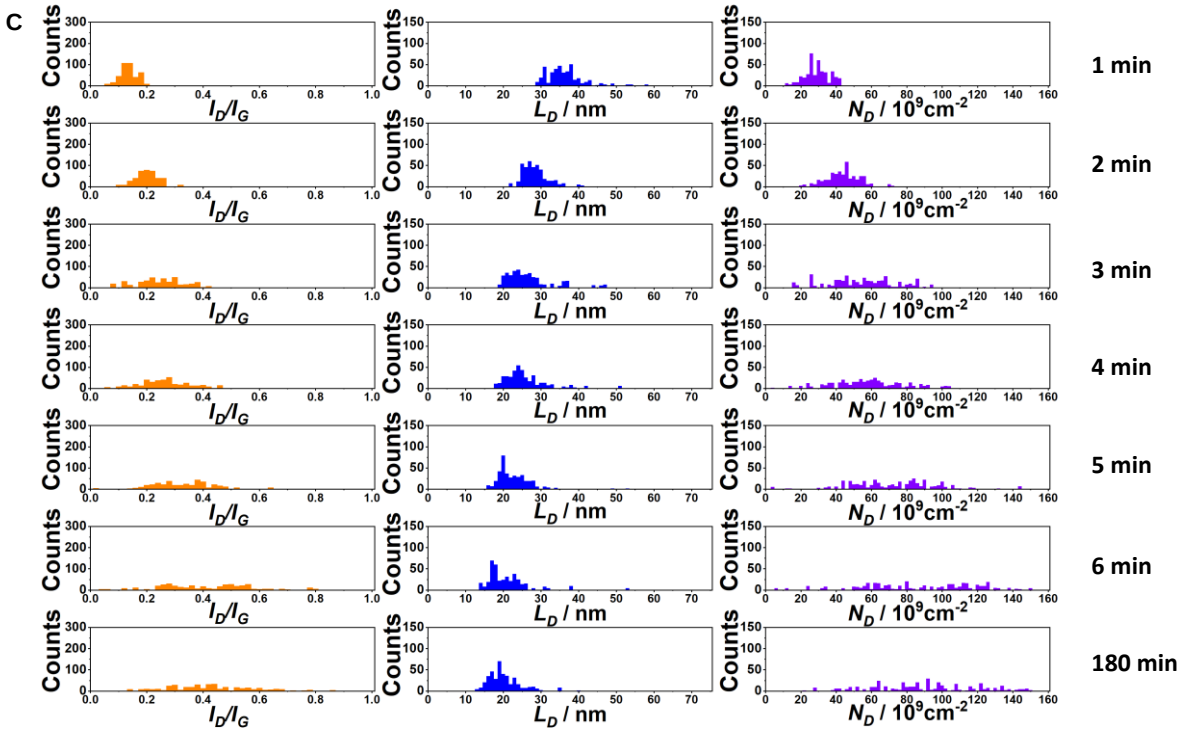

Fig. 7 Histograms of Raman I_D/I_G (left) L_D (middle), and n_D (right) of (A) G/SiO_2/Si, (B) G/Cu, (C) G/Ni after reacting with MAH at 150 °C for different lengths of time. For each set, ~400 data points were collected from 2 independent samples.

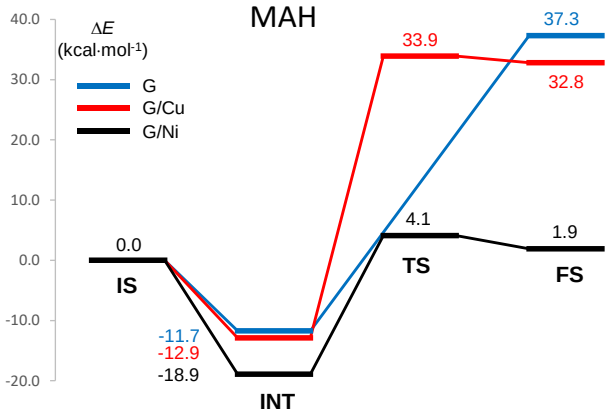

Fig. 8 Reaction energy profiles for the Diels-Alder reaction between MAH and G (blue), G/Cu (red) or G/Ni (black). Molecular representations for each G/Ni stationary point are given.

interacting Ni substrate leads to a substantially lower predicted energy barrier. The energy barrier of the G system could not be definitively determined as the transition state due to the high endothermicity and close resemblance between the TS and FS. The bond formation in the G/Ni system is significantly more asynchronous (Δd=0.37Å for Ni and Δd=0.10Å for Cu where Δd is the difference in length of the forming bonds) than in either the G/Cu case which are nearly synchronous (Fig. 10. See figure S22 for the reaction path). The enhanced stability in the product with Ni is partially reflected in the decreased forming bond distances (Fig. 10). The trend in activation energy is in agreement with the experimental trend, but the differences between each system are smaller in the experimental values, for which a plausible rationalization is posited separately.

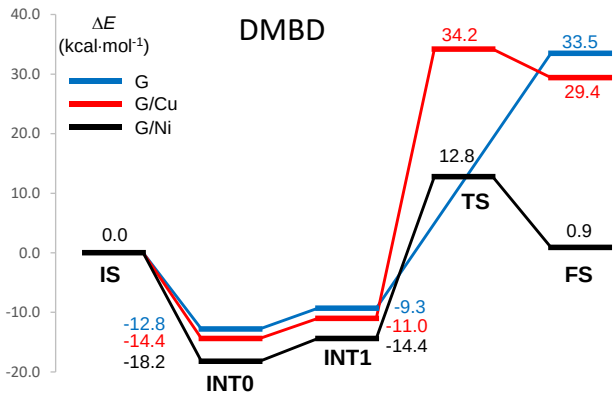

Fig. 9 Reaction energy profiles for the Diels-Alder reaction using DMBD with G(blue), G/Cu (red) and G/Ni (black). Molecular representations for each G/Ni stationary point are are given.

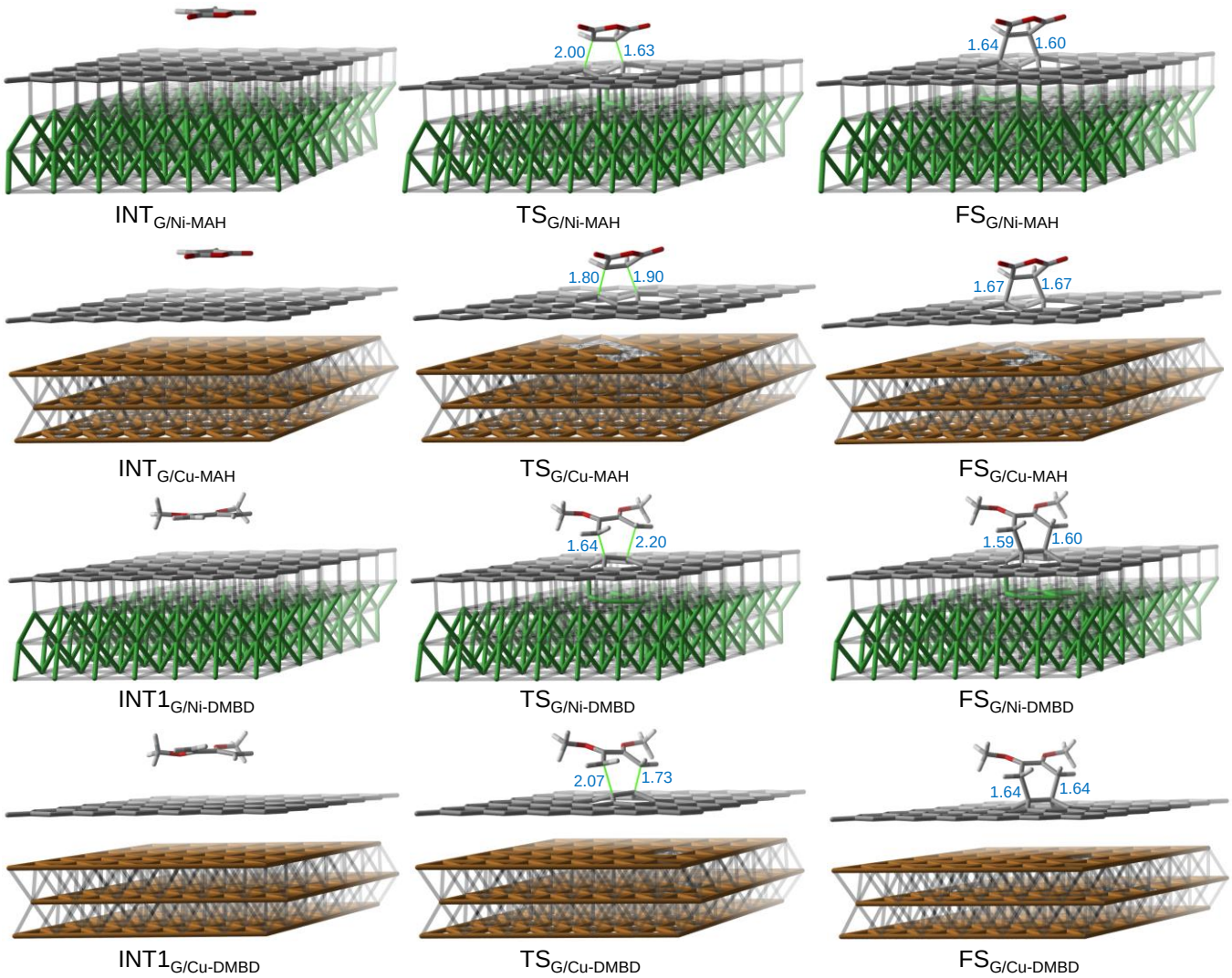

Fig. 10 Calculated geometries for the stationary points INT, INT1, TS, and FS using reactants MAH and DMBD with graphene on Cu and Ni substrates. The C-C bond lengths are provided in units of angstroms.

The energy profile for the DA reaction with DMBD (Fig. 9) follows a similar trend to the DA reaction with MAH. Trans-DMBD physisorbs similarly to G/Cu and G systems (INT0) to that with MAH, however the physisorption is slightly weaker than in the MAH case using the G/Ni system, by 0.7 kcal·mol^{-1}. The trend of *cis*-DMBD physisorbs to each system (INT1) is similar as INT0. The trend in activation energy from INT1 is predicted to be slightly different with G/Ni having the lowest barrier (27.1 kcal·mol^{-1}) followed by G/Cu (45.2 kcal·mol^{-1}). While the activation energy from INT1 is slightly greater for G/Cu as compared with G, the energy from IS is lower for G/Cu and the overall reaction is less thermodynamically unfavorable than with G. A summary of the overall energetics is provided in Table 1. The reaction is again more asynchronous using Ni, and enhanced product stability using Ni is reflected in the decreased forming bond lengths (Fig. 10).

Table 1 Reaction and activation energies for the DA reactions with MAH and DMBD with G, G/Cu, and G/Ni. Energies are reported with both the initial state (IS) and lowest energy intermediate (INT) as references. All energies are listed in units of kcal·mol^{-1}.

	ΔE_{IS}	ΔE_{INT}	$\Delta E^{\ddagger}_{IS}$	$\Delta E^{\ddagger}_{INT}$
G_MAH	37.3	49.0	-	-
G/Cu_MAH	32.8	45.7	33.9	46.8
G/Ni_MAH	1.9	20.8	4.1	23.0
G_DMBD	33.5	46.3	-	-
G/Cu_DMBD	29.4	43.8	34.2	48.6
G/Ni_DMBD	0.9	19.1	12.8	31.0

A basic understanding of the nature of the physisorption in INT can be used in part to rationalize the trend in activation energy. Charge density difference surfaces of the adsorbed MAH or DMBD were constructed according to the following equation,

$$\Delta\rho(r) = \rho_{graphene/reagent}(r) - (\rho_{graphene}(r) + \rho_{reagent}(r)) \quad (3)$$

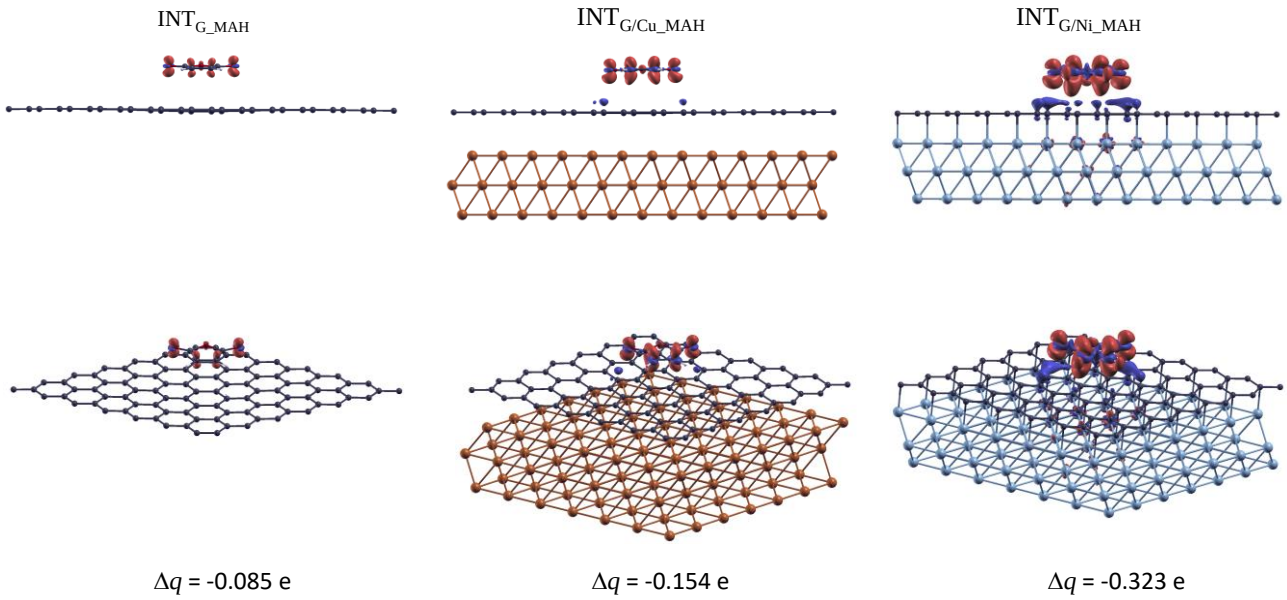

Fig. 11 Charge density difference plots of $INT_{G,}$ $INT_{G/Cu}$, and $INT_{G/Ni}$ for MAH. Charge transfers (Δq) are determined from a Bader charge analysis of the electron densities.

where $\rho_{graphene/reagent}$(r), $\rho_{graphene}$ (r), and $\rho_{reagent}$(r) are the electron densities of the graphene/reagent, free standing graphene, and free reagent respectively. The surfaces reveal the extent and direction of charge transfer upon complexation. With MAH, a net charge transfer from graphene to the electron deficient MAH would be expected, which is observed. Substantially greater charge is transferred from the graphene to MAH in the G/Cu system compared to just free-standing graphene, G, and greater still in the G/Ni system (cf. Δq_G = −0.085*e*, $\Delta q_{G/Cu}$ = −0.154*e* and $\Delta q_{G/Ni}$ = −0.323*e*). This charge transfer is likely a consequence of stronger $HOMO_{G/M}$→$LUMO_{MAH}$ interaction which causes a reduction in the activation energy. With DMBD used as the dienophile, the charge transfer is close to zero in each substrate case (Fig. S21). The interaction in INT is then likely a combination of dispersion interactions and charge transfer in each direction from graphene to electron rich DMBD and from DMBD to graphene leading to a net overall charge transfer close to zero, yet still contributing to the interaction. Ultimately, the buildup of charge on the graphene surface donated from the strongly interacting Ni leads to a lower energy bond formation.

The results are in agreement with the observed rate trends. However, each case is predicted to not be thermodynamically favorable, with G/Ni being nearly thermoneutral. It is plausible that the reaction could occur at sites with greater curvature and distortion than the idealized flat systems explored here, which may lead to more favorable thermodynamic predictions.[43-45] At these distorted sites, the substrate would exhibit weaker interactions with the graphene surface, thus attenuating substrate differences leading to predicted energy changes that would be less than in the flat systems explored here where the graphene-substrate interaction is the strongest.

Conclusions

In this work, we investigated the impact of a metal substrate on the reactivity of graphene, both experimentally and computationally. Reactions with DMBD or MAH at different temperatures all exhibited substrate-dependent behaviors, supporting our hypothesis that a metal substrate enhances the reactivity of graphene towards DA reactions. The G/Ni system is especially encouraging, giving the highest reactivity and degree of functionalization among the graphene/substrate systems and about twice higher rates than G/SiO_2/Si.

The results from computation largely support the experimentally obtained rate trends with substrate. The enhanced reactivity observed with the electron rich Ni substrate is rationalized by stronger $HOMO_{G/Ni}$→$LUMO_{MAH}$ frontier orbital interactions with MAH and slightly more favorable thermodynamics with DMBD. Incorporation of the effects of roughness in the graphene surface is expected to lead to reactivity enhancement. More systematic investigations into the effects of curvature of the graphene surface while adhered to metallic substrates, both experimentally and theoretically, are currently underway, and results will be reported in a future account.

Experimental

Materials

Maleic anhydride, 2,3-dimethoxy butadiene, urea, ethanol (200 proof, purity: >99.5%), phosphoric acid, isopropanol, poly(methyl methacrylate) (MW 960,000), were purchased from Sigma-Aldrich. Acetone (purity: >99.5%) was obtained from Fisher Scientific. *p*-Xylene (purity: 99%) was supplied by Sigma-Aldrich. All reagents were used as received unless

otherwise noted. Ultrapure water was obtained from a Millipore Milli-Q® Direct 16 Water Purification System. Silicon wafers with a 300 nm thick SiO_2 layer were purchased from MTI Corp. Cu foils (25 µm thick, purity: > 99.8 wt%) were purchased from Alfa Aesar. Cu and Ni metals, both of 99.99% purity, were purchased from Kurt J. Lesker Company.

Fabrication of Ni and Cu substrates

Silicon wafers were ultrasonicated in Milli-Q water for 1 h, followed by rinsing with acetone and isopropanol. After drying in air, the silicon wafer was transferred to an electron beam evaporator (Solution Process Development System, CHA Industries), equipped with a tungsten filament emitter and SIMATIC Siemens Manager S7 Version 5.4 software. With the pressure maintained at ~10^{-6} – ~10^{-7} torr, Ni or Cu film (thickness of 100 nm) was deposited on the silicon wafer at the rate of 2 Å per second. The products were stored under the N_2 atmosphere.

Fabrication of CVD graphene on Cu foil

CVD graphene was fabricated on a home-built CVD apparatus equipped with a Lindberg/Blue M (TF55030A-1) furnace, a quartz tube (SentroTech) and CH_4/H_2/Ar gas system. The Cu foil was cut to strips of dimension ~6 cm × ~2.5 cm each and was then subjected to electropolishing in a direct current generator (Keithley 2614b) for 30 – 45 s to clean the surface and to reduce the roughness of the surface. Cu strips served as both the cathode and the cathode, and the electrolyte solution was prepared from ultrapure water (500 mL), phosphoric acid (250 mL), ethanol (250 mL), isopropanol (50 mL), and urea (5 g). The cleaned Cu strips were rinsed thoroughly with ultrapure water to remove excess electrolytes and dried under N_2. The clean Cu strips were then placed in the tube furnace, and the tube was evacuated to the base pressure < 50 mTorr. The temperature was raised to 1000 °C for a duration of 60 minutes under H_2 (4 sccm). H_2 (4 sccm) and CH_4 (0.4 sccm) were subsequently introduced into the tube furnace at 1000 °C for 30 minutes, and the furnace was allowed to cool under same gas mixture for 60 min. CVD graphene on Cu foil was retrieved from the furnace after cooling to room temperature.

Transfer of CVD graphene to a new substrate

The CVD graphene on Cu foil was transferred to Ni, Cu or silicon wafer using the PMMA-assisted method.[32, 46] Briefly, the CVD graphene on Cu foil was spin-coated with a solution of PMMA in acetone (300 µL, 40 mg/mL) at 500 rpm for 1 min to form a protective film on graphene. The Cu foil was then etched away by immersing the sample in a solution of $FeCl_3$ in 1 M HCl (3 M) for 1 h, followed by washing with ultrapure water for 3 times. The new substrate (Ni, Cu or silicon wafer) was then placed on top of graphene. After drying in air overnight, the sample was soaked in acetone for 5 h to remove PMMA film, rinsed with acetone and air dried.

Diels-Alder Reaction on substrate-supported graphene

A solution of DMBD or MAH in *p*-xylene (10 µL, 0.1 M) was dropped on graphene. Reaction was carried out under heating in an oven at 50, 100, or 150 ^{o}C for 1, 2, 3, 4, 5, 6, or 180 min. The samples were washed with acetone for 3 times to remove the residual reagents and were dried under air flow. For Raman characterization, graphene supported on Ni or Cu were transferred to silicon wafers, following the PMMA-assisted transfer procedure described above.

Raman characterization

Spot Raman spectra were collected on a Bruker SENTERRA II Raman microscope, equipped with an Olympus BX optical microscope (50× objective lens), a motorized X, Y, Z sampling stage, and a thermo-electrically cooled charge-coupled device (CCD) detector. An argon laser was used at 532 nm excitation (2.33 eV), with the power set at below 1 mW. Each spot spectrum was recorded in the wavenumber range of 35 – 4400 cm^{-1}, obtained after 30 times of scanning for about 30 s. The spectral resolution was 0.5 cm^{-1}. Data acquisition and instant spectrum inspection were done using the OPUS software.

Automatic spatial mapping was conducted on an NT-MDT Raman microscope equipped with an Andor Technology CCD camera at 532 nm excitation using a He-Ne laser. Samples were placed on an x-y positional piezoelectric objective stage, and an area of 10 µm × 10 µm (100 points, exposure time of 4 s for each scanning point) was used for signal acquisition. The spectra cover the wavenumber range of 933 – 4200 cm^{-1} with the resolution of 4 cm^{-1}. Data acquisition and the instant spectrum visualization were done using the Nova Px software.

The wavenumber at the maximum peak height was the peak position of the *D*, *G* or *2D* band. The peak intensity, I_D, I_G or I_{2D}, was obtained by integrating the area under each peak after subtracting the background. The spectral ranges were set at 1290 – 1420 cm^{-1}, 1540 – 1620 cm^{-1} and 2560 – 2780 cm^{-1} for *D, G* and *2D* bands, respectively.

Computational

Density functional theory (DFT) was used to reveal the origins of the substrate enhanced Diels-Alder reactivity observed. Spin polarized DFT was used for all calculations using Ni(111) and systems in the triplet configuration. All DFT calculations were performed using the Plane-Wave Self Consistent Field (PWSCF) plane wave code within the Quantum Espresso package.[47] The generalized gradient approximation (GGA) was applied using the Perdew-Burke-Ernzerhof, PBE,[42] functional augmented with the DFT-D2[48] dispersion correction. Ultrasoft pseudopotentials were used for describing the interaction between the ionic core and the valence electrons. A gaussian smearing parameter of 0.002 Ry was used for brillouin-zone integration in calculations using Cu or Ni. All geometry optimizations (relax) were performed using a Monkhorst-pack 1x1x1 k-point grid while all electron densities and final reported SCF energies were determined using a 3x3x1 k-point grid. The kinetic energy cutoffs for the charge density and wavefunctions were 400 Ry and 40 Ry respectively using the 3x3x1 k-point grid. The supercell consisted of a 6 x 6 graphene

sheet with and without a three-layer Cu and Ni slab where the bottom layer of the metal slab was fixed in all geometry optimizations. A vacuum space of 15 Å normal to the bottom metal layer was applied. Using this method, the graphene lattice parameter obtained was 2.48 Å, which is reasonably close to the experimental value. Transition states were obtained by investigating the minimum energy path using the climbing image elastic band (CI-NEB) method[49, 50] All energies are available in Table S1.

Author Contributions

We strongly encourage authors to include author contributions and recommend using CRediT for standardised contribution descriptions. Please refer to our general author guidelines for more information about authorship.

Conflicts of interest

There are no conflicts to declare.

Acknowledgements

The authors are grateful to the financial support from the National Science Foundation (CHE-1112436 to M.Y. and L.M.W.; CBET-2028826 to H.L.).

Notes and references

1 M. J. Allen, V. C. Tung and R. B. Kaner, *Chem. Rev.* , 2010, **110**, 132-145.
2 V. Georgakilas, M. Otyepka, A. B. Bourlinos, V. Chandra, N. Kim, K. C. Kemp, P. Hobza, R. Zboril and K. S. Kim, *Chem. Rev.*, 2012, **112**, 6156-6214.
3 X. Huang, X. Qi, F. Boey and H. Zhang, *Chem. Soc. Rev.*, 2012, **41**, 666-686.
4 J. Park, T. Jin, C. Liu, G. Li and M. Yan, *ACS Omega*, 2016, **1**, 351-356.
5 J. Park, X. Yang, D. Wickramasinghe, M. Sundhoro, N. Orbey, K.-F. Chow and M. Yan, *RSC Adv.*, 2020, **10**, 26486-26493.
6 J. Park, H. S. N. Jayawardena, X. Chen, K. W. Jayawardana, M. Sundhoro, E. Ada and M. Yan, *Chem. Commun.*, 2015, **51**, 2882-2885.
7 J. Park and M. Yan, *Acc. Chem. Res.*, 2013, **46**, 181-189.
8 J. Bai, X. Zhong, S. Jiang, Y. Huang and X. Duan, *Nat. Nanotechn.*, 2010, **5**, 190-194.
9 Y. Lin, Y. Liao, Z. Chen and J. W. Connell, *Mater. Res. Lett.*, 2017, **5**, 209-234.
10 Q. Wu, Y. Wu, Y. Hao, J. Geng, M. Charlton, S. Chen, Y. Ren, H. Ji, H. Li, D. W. Boukhvalov, R. D. Piner, C. W. Bielawski and R. S. Ruoff, *Chem. Commun,*, 2013, **49**, 677-679.
11 Q. H. Wang, Z. Jin, K. K. Kim, A. J. Hilmer, G. L. C. Paulus, C.-J. Shih, M.-H. Ham, J. D. Sanchez-Yamagishi, K. Watanabe, T. Taniguchi, J. Kong, P. Jarillo-Herrero and M. S. Strano, *Nat. Chem.*, 2012, **4**, 724-732.
12 M. A. Kim, N. Qiu, Z. Li, Q. Huang, Z. Chai, S. Du and H. Liu, *Adv. Funct. Mater.*, 2020, **30**.
13 H. C. Kolb, M. G. Finn and K. B. Sharpless, *Angew. Chem. Int. Ed.*, 2001, **40**, 2004-2021.
14 J. M. Englert, C. Dotzer, G. Yang, M. Schmid, C. Papp, J. M. Gottfried, H.-P. Steinruck, E. Spiecker, F. Hauke and A. Hirsch, *Nat. Chem.*, 2011, **3**, 279-286.
15 L. Zhang, L. Zhou, M. Yang, Z. Liu, Q. Xie, H. Peng and Z. Liu, *Small*, 2013, **9**, 1134-1143.
16 S. Sarkar, E. Bekyarova, S. Niyogi and R. C. Haddon, *J. Am. Chem. Soc.* , 2011, **133**, 3324-3327.
17 S. Bian, A. M. Scott, Y. Cao, Y. Liang, S. Osuna, K. N. Houk and A. B. Baraunschweig, *J. Am. Chem. Soc.* , 2013, **135**, 9240-9243.
18 Y. Cao, S. Osuna, Y. Liang, R. C. Haddon and K. N. Houk, *J. Am. Chem. Soc.* , 2013, **135**, 17643-17649.
19 P. P. Brisebois, C. Kuss, S. B. Schougaard, R. Izquierdo and M. Siaj, *Chem. Eur. J.*, 2016, **22**, 5849-5852.
20 P. A. Denis, *Chem. Eur. J.*, 2013, **19**, 15719-15725.
21 J. Li, M. Li, L. L. Zhou, S. Y. Lang, H. Y. Lu, D. Wang, C. F. Chen and L. J. Wan, *J. Am. Chem. Soc.*, 2016, **138**, 7448-7451.
22 S. J. Altenburg, M. Lattelais, B. Wang, M.-L. Bocquet and R. Berndt, *J. Am. Chem. Soc.*, 2015, **137**, 9452-9458.
23 L. Daukiya, C. Mattioli, D. Aubel, S. Hajjar-Garreau, F. Vonau, E. Denys, G. Reiter, J. Fransson, E. Perrin, M.-L. Bocquet, C. Bena, A. Gourdon and L. Simon, *ACS Nano*, 2017, **11**, 627-634.
24 P. A. Khomyakov, G. Giovannetti, P. C. Rusu, G. Brocks, J. van den Brink and P. J. Kelly, *Phys. Rev. B: Condens. Matter Mater. Phys.*, 2009, **79**, 195425/195421-195425/195412.
25 Y. Gamo, A. Nagashima, M. Wakabayashi, M. Terai and C. Oshima, *Surf. Sci.*, 1997, **374**, 61-64.
26 A. Dahal and M. Batzill, *Nanoscale*, 2014, **6**, 2548-2562.
27 D. E. Parreiras, E. A. Soares, G. J. P. Abreu, T. E. P. Bueno, W. P. Fernandes, V. E. de Carvalho, S. S. Carara, H. Chacham and R. Paniago, *Phys. Rev. B*, 2014, **90**, 155454.
28 C. Gong, G. Lee, B. Shan, E. M. Vogel, R. M. Wallace and K. Cho, *J. Appl. Phys.*, 2010, **108**.
29 X. Yang, F. Chen, M. A. Kim, H. Liu, L. M. Wolf and M. Yan, *Chem. Eur. J.*, 2021.
30 S. Sarkar, E. Bekyarova, S. Niyogi and R. C. Haddon, *J. Am. Chem. Soc.*, 2011, **133**, 3324-3327.
31 I. I. Suni and B. Du, *IEEE Trans. Semicond. Manuf.*, 2005, **18**, 341-349.
32 X. Yang and M. Yan, *Nano Res.*, 2020, **13**, 599-610.
33 M. S. Dresselhaus, A. Jorio, M. Hofmann, G. Dresselhaus and R. Saito, *Nano Lett.*, 2010, **10**, 751-758.
34 A. C. Ferrari, *Solid State Comm.*, 2007, **143**, 47-57.
35 J.-M. Seo and J.-B. Baek, *Chem. Commun.* , 2014, **50**, 14651-14653.
36 J. Lee, S. Shim, B. Kim and H. S. Shin, *Chem. Eur. J.*, 2011, **17**, 2381-2387.
37 A. C. Ferrari and D. M. Basko, *Nat. Nanotechn.*, 2013, **8**, 235.
38 L. G. Cançado, A. Jorio, E. H. M. Ferreira, F. Stavale, C. A. Achete, R. B. Capaz, M. V. O. Moutinho, A. Lombardo, T. S. Kulmala and A. C. Ferrari, *Nano Lett.*, 2011, **11**, 3190-3196.
39 E. H. Ferreira, M. V. O. Moutinho, F. Stavale, M. M. Lucchese, R. B. Capaz, C. A. Achete and A. Jorio, *Phys. Rev. B*, 2010, **82**, 125429.
40 B. Hammer, L. B. Hansen and J. K. Nørskov, *Physical Review B*, 1999, **59**, 7413-7421.
41 M. Ernzerhof and G. E. Scuseria, *The Journal of Chemical Physics*, 1999, **110**, 5029-5036.
42 J. P. Perdew, K. Burke and M. Ernzerhof, *Physical Review Letters*, 1996, **77**, 3865-3868.
43 S. Osuna and K. N. Houk, *Chemistry – A European Journal*, 2009, **15**, 13219-13231.
44 C. Riplinger, P. Pinski, U. Becker, E. F. Valeev and F. Neese, *The Journal of Chemical Physics*, 2016, **144**, 024109.
45 B. Willocq, V. Lemaur, M. El Garah, A. Ciesielski, P. Samorì, J. M. Raquez, P. Dubois and J. Cornil, *Chemical Communications*, 2016, **52**, 7608-7611.

46 J. W. Suk, A. Kitt, C. W. Magnuson, Y. Hao, S. Ahmed, J. An, A. K. Swan, B. B. Goldberg and R. S. Ruoff, *ACS Nano*, 2011, **5**, 6916-6924.
47 P. Giannozzi, S. Baroni, N. Bonini, M. Calandra, R. Car, C. Cavazzoni, D. Ceresoli, G. L. Chiarotti, M. Cococcioni, I. Dabo, A. Dal Corso, S. de Gironcoli, S. Fabris, G. Fratesi, R. Gebauer, U. Gerstmann, C. Gougoussis, A. Kokalj, M. Lazzeri, L. Martin-Samos, N. Marzari, F. Mauri, R. Mazzarello, S. Paolini, A. Pasquarello, L. Paulatto, C. Sbraccia, S. Scandolo, G. Sclauzero, A. P. Seitsonen, A. Smogunov, P. Umari and R. M. Wentzcovitch, *Journal of Physics: Condensed Matter*, 2009, **21**, 395502.
48 S. Grimme, *Journal of Computational Chemistry*, 2006, **27**, 1787-1799.
49 G. Henkelman and H. Jónsson, *J. Chem. Phys.*, 2000, **113**, 9978-9985.
50 G. Henkelman, B. P. Uberuaga and H. Jónsson, *J. Chem. Phys.*, 2000, **113**, 9901-9904.